# CHAPTER TWO

LITERATURE REVIEW

2.1 Introduction

This chapter presents the literature review on the carbon nanotubes, CNT/polymer and CNT/metal oxide composites along with their application as alcohol sensors. An overview on the fabrication techniques to prepare CNT is discussed in Section 2.2. Section 2.3 covers the novel properties of carbon nanotubes. The application of polymer and metal oxide composites with carbon nanotubes as alcohol sensors is presented in Section 2.4. The general application of carbon nanotubes as sensors is illustrated in Section 2.5. The utilized instruments for the characterization of carbon nanotube composites and example for each method are explained in Sections 2.6 and Section 2.7 respectively.

2.2 Introduction Carbon Nanotubes (CNTs):

The discovery of carbon nanotubes (CNTs) has generated keen interest among researchers to develop CNT-based sensors for many applications. The application of CNTs in next-generation of sensors has the potential of revolutionizing the sensor industry due to

their inherent properties such as small size, high strength, high electrical and thermal conductivity, as well as high specific surface area. CNTs are hexagonal networks of carbon atoms of approximately 1 nm diameter and 1 to 100 microns of length. They can essentially be thought of as a layer of graphite rolled-up into a cylinder. Depending on the arrangement of their graphene cylinders, there are two types of nanotubes: single-walled nanotubes (SWNTs) and multi-walled nanotubes (MWNTs). SWNTs have only one single layers (approximately 50), as shown in Figure 2.1. Furthermore, the films of synthesized CNTs can be aligned or random in nature.
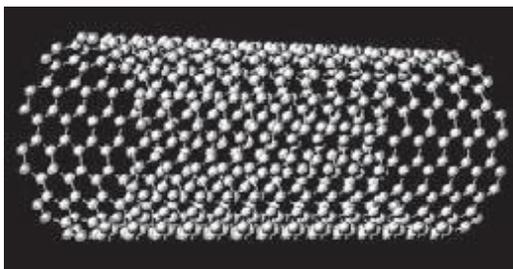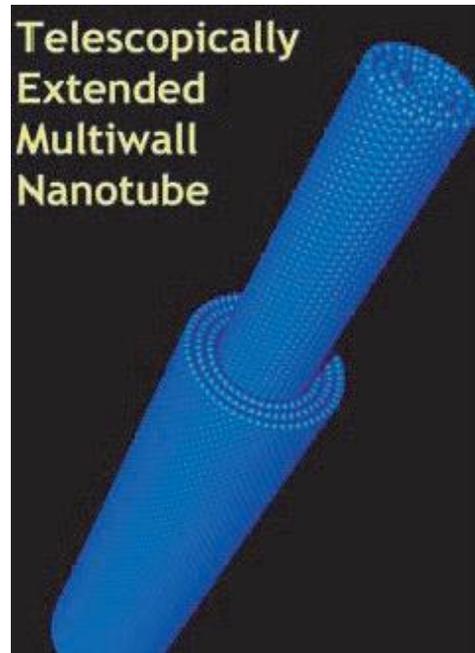
<table>
<tr><td>(a)</td><td>(b)</td></tr>
</table>

Figure 2.1: Displays structure of SWNTs as shown in (a) and structure of MWCNTs as shown in (b).

2.2.1 Synthesis of carbon nanotubes:

Generally, three techniques are being used for producing CNTs, namely:-

(i)   Carbon arc-discharge technique.

(ii)   Laser-ablation technique.

(iii)   Chemical vapor deposition (CVD) technique.

In 1991, MWNTs were first discovered by [1] arc-discharge technique when fine threads in a bit of shoot under electron microscope have been observed. The strands were extremely thin and long tubes of pure carbon SWNTs were synthesized for the first time in 1996 utilizing metal catalyst in arc-discharge method [2]. Laser-ablation technique was used to produce bundles of aligned SWNTs. Afterward; the catalytic growth of MWNTs by CVD was proposed [3]. The three mentioned above techniques are presented and discussed in further detail in the next sections below.

(i)   Carbon Arc-Discharge Technique: -

Two carbon electrodes are used in the carbon arc-discharge technique to generate an arc by DC current. The electrodes are kept in vacuum chamber and an inert gas is supplied to the chamber. The purpose of the inert gas is to increase the speed of carbon deposition. Initially, the two electrodes are kept independent. Once the pressure is stabilized, the power supply is turned on (about 20 V) and the positive electrode is then gradually brought closer to the negative electrode to strike the electric arc. On arcing, the electrodes

become red hot and a plasma forms. Once the arc stabilizes, the rods are kept about a millimeter apart while the CNT deposits on the negative electrode. The power supply is cut-off and the machine is left for cooling once a specific length is reached. The two most important parameters to be taken care of in this method are: -

(i)   The control of arcing current and

(ii)   The optimal selection of inert gas pressure in the chamber.

Arc- discharge technique produces high quality CNTs. While SWNTs can only be grown in presence of a catalyst, MWNTs do not need a catalyst for growth. MWNTs can be obtained by controlling the pressure of inert gas in the discharge chamber and the arcing current. The by-products are polyhedron shaped multi-layered graphitic particles in case of MWNTs. High quality MWNTs having diameters ranging from 2 to 20 nm and length of several microns at the gram level [4]. A potential of approximately 18 V and a helium pressure of about 500 Torre were applied. Analysis by transmission electron microscopy (TEM) revealed that the nanotubes consisted of two or more carbon shells. The MWNTs produced by arc-discharge method were highly crystalline and were bound together by strong van der Waals forces. SWNTs with diameters ~1 nm were synthesized by a group of researchers [2] using a gas mixture of 10 Torr methane and 40 Torr argon at a DC current of 200 A and a voltage of 20 V. Bethune carried out the experiment using Co, Ni, and Fe as catalysts to synthesize CNTs by using carbon as anode at currents between 95 to 105 A and He pressures between 100 to 500 Torr. The TEM analysis revealed that SWNTs

of diameters 1.2±0.1nm were obtaind only with Co catalysts [5]. Optimized the SWNT growth by arc-discharge technique by using graphite cathode (16 mm diameter, 40mm long), graphite anode (6 mm diameter, 100 mm long), mixture of catalysts (Ni-Co, Co-Y, or Ni-Y), along with helium pressure of 660 mbar , arcing current of 100 A, and voltage drop of 30 V between the electrodes. The deposited material consisted of high amount of entangled carbon ropes of diameters 5-20 nm as revealed by scanning electron microscopy (SEM). Recently, CNTs have been synthesized by arc-discharge in open air.

(ii)   Laser-Ablation Technique

To make the most of the laser-ablation technique for producing CNTs, intense laser pulses are utilized to ablate a carbon target. The pulsed laser-ablation of graphite in the presence of an inert gas and catalyst forms CNTs has been used by many researchers of the same interest [6]. The X-ray diffraction (XRD) and transmission electron microscopy revealed that the SWNTs have been successfully produced by other group which has been described elsewhere [6]. Using laser-ablation were ropes (or bundles) of 5 to 20 nm diameter and tens to hundreds of microns of length. This report [7] has found that individual nanotubes of lengths tens of microns are formed in the vicinity of the target at the beginning. These nanotubes subsequently coalesce into bundles. Based on spectral emission and laser-induced fluorescence measurements, it was suggested [8] that the carbon for nanotube formation comes from direct ablation as well as from carbon particles suspended in the reaction zone. It was also proposed by the same group [8] that the

confinement of the nanotubes in the reaction zone within the laser beam allows the nanotubes to be purified and annealed during the formation process by laser heating. SWNTs and other nanotublar structures (graphite nanocages and low aspect ratio nanotubeles) were synthesized other researchers at the same field of interest [9]. By pulsed KrF laser-ablation of a graphite pellet at 500 Torr argon pressure, 1150 ºC temperature, and a laser intensity of 8×10^8 W/cm^2. It was observed that relatively high UV laser intensity detrimental to the growth of SWNTs [10]. Synthesizing multi-layered MWNTs having tip angle of 15-20$^°$ by using high vacuum laser-ablation, graphite powder was dispersed on a Si (100) wafer substrate and CNTs were grown selectively at high substrate temperature.

In general, some of major parameters that determine the amount of produced CNTs are: the amount and type of catalysts, laser power and wavelength, temperature, pressure, type of present inert gas, and the fluid dynamics near the carbon target. When synthesizing SWNTs, the byproducts in case of arc-discharge and laser-ablation techniques are fullerenes, graphitic polyhedrons with enclosed metal particles, and amorphous carbon.

(iii)   Chemical Vapor Deposition(CVD) Technique

Chemical vapor deposition, CVD is a very versatile process used in the production of coatings, powders, fibers and monolithic parts. With CVD, it is possible to produce almost any metallic and non-metallic elements, including carbon and silicon. The CNTs are synthesized by impart energy to hydrocarbons, the imparted energy breaks the

molecule into reactive radical species at a temperature ranging from 550 ˚C to 750 ˚C. These reactive species then diffused down to the substrate, which is heated and coated in a catalyst (usually a first row transition metal such as Ni, Fe or Co) where it remains bonded. The outcome of this process is the formation of CNTs. The commonly used hydrocarbon sources are methane, ethylene, and acetylene; while the commonly used energy sources are electron beam and resistive heating. Microtubules of up to 50 µm length of CNTs were synthesized by others [11]. The synthesized materials have been achieved by utilizing catalytic decomposition of acetylene over iron particles at 700 ºC. Iron nanoparticles (embedded in mesoporous) as catalyst for large-scale synthesis of aligned CNTs have been put in used. The tubes were about 50µm long and well graphitized. A CVD technique using microwave energy for synthesizing MWNTs was developed group of researchers [12]. They used acetylene as the hydrocarbon and cobalt as the catalyst at acetylene at a temperature of 700 ºC. MWNTs prepared by this process had an average diameter of 20 to 30 nm and consisted of 26 layers. A sequential combination of radio frequency plasma enhanced CVD (RF PECVD) and thermal CVD was also utilized other group [13]. CNTs were synthesized on stainless steel plates from acetylene and hydrogen gas mixture [14]. Synthesized dense networks of SWNTs using Ni catalyst layer of 0.2 nm thick by thermal CVD at temperatures as low as 600 ºC. Based on the interaction between the catalyst and its support growth model for CVD synthesis was proposed. It has been found that, the fastest growth rates of SWNTs during CVD synthesis

can only be explained by surface diffusion of hydrocarbons on the catalyst support or along the CNTs [15]. Used metal (Fe)-encapsulated dendrimers as catalysts for low-temperature growth of CNTs. MWNTs were synthesized at 175 ℃ via decomposition of carbon tetrachloride in supercritical carbon dioxide. CVD technique with gas-phase catalyst delivery was used other group of researchers [16]. To direct the assembly of carbon nanotubes in a variety of predetermined orientations, building them into one-, two-, and three-dimensional arrangements. This could be useful in the manufacture of electromechanical devices.

There are several parameters that affect the synthesis of CNTs by CVD technique. The key parameters are the nature of hydrocarbons, catalysts, and the growth temperature. Most of the CVD techniques utilize ethylene and acetylene as hydrocarbons for synthesizing MWNTs. It was observed that both SWMNs and MWNTs can be synthesizing by optimizing the catalyst [17]. By optimizing the growth conditions, they synthesized SWNTs of diameter 0.65 nm at a substrate temperature of 660 ℃. With regards to the effect of temperature, the density and growth rate of CNTs increase as the temperature increases. Also, the CNTs tend to be vertically aligned as the temperature increases. Taguchi analytical model has been applied to optimize the effective parameters of CVD for controlling the production of CNTs [18]. Quantitative contributions of process parameters as well as optimum factor levels have been obtained using analysis of variance (ANOVA) and analysis of mean (AOM), respectively. Although excellent alignment and

positional control on the nanometer scale can be achieved with the CVD technique, there are high defect thermal densities in the MWNT structures grown by this process. It is most likely due to the lack of sufficient thermal energy for annealing CNTs because of relatively low growth temperature.

A comparison among these three CNT synthesis techniques indicates that arc-discharge and laser-ablation methods produce high percentage (>70%) and quality of CNTs. Moreover, the cost of producing CNTs by arc-discharge method is cheaper. Nevertheless, the main disadvantages with these processes are: -

(i)   Tangled CNTs are synthesized that make the purification and applications of CNTs difficult.

(ii)   These processes rely on evaporation of carbon atoms at temperatures >3000 °C.

However, it is worth mentioning that in addition to materials scale-up, CVD technique offers controlled synthesis of aligned and ordered CNTs. Although the microstructure of the CNTs tips synthesized by CVD technique have well-formed caps compared to other techniques, they often have interrupted graphite layers. In applications such as scanning probe microscopy, tips are very important. Even though CVD process appears technologically easier, the required quality of tips can be made by arc-discharge method.

2.3 Properties of Carbon Nanotubes

The unique and extremely important properties of CNTs make them of great potential application. For instance, CNTs can be used as filters for filtration of bacterial contaminants such as *Escherichia coli* from water and heavy hydrocarbons from petroleum because of their exceptional thermal and mechanical stability as well as high surface area. Even though SWNTs are structurally similar to single layer of graphite (that is a semiconducting with zero band gap), they can be either metallic or semiconducting depending upon the tube diameter and the chirality (the sheet direction in which the graphite sheet is rolled to form a nanotube cylinder). Let us introduce lattice translation vector L. A nanotube can be constructed in such a way that the hexagon at a position L can be rolled onto a hexagon at the origin. L is called the chiral vector and becomes the circumference of the nanotube. The directional angle η of L is called the chiral angle as shown in Figure 2. Because each translation vector is written as $L = n_a a + n_b b$ with a and b being the primitive translation vectors, the structure of a nanotube is specified by the set of integers n_a and n_b. The axis is perpendicular to L, which typically results in a nanotube with a helical structure. There are some exceptions to this, including nonhelical nanotubes, zigzag nanotubes with $\eta = 0$ and armchair tubes with $\eta = \pi/6$. Other helical tubes are called chiral nanotubes. Because the stability is mainly determined by their thickness or circumference, the direction of L for grown nanotubes is distributed almost uniformly.
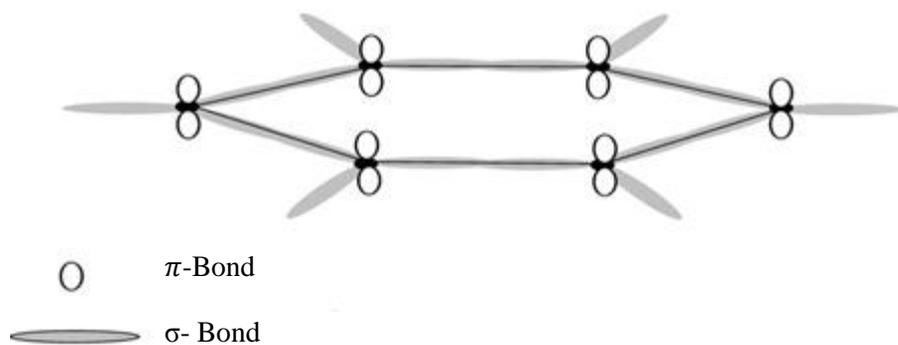
Figure 2.2: Basic hexagonal bonding structures for one graphite layer (the 'graphene sheet'). Carbon nuclei shown as filled circle, out-of-plane π-bonds, and σ-bonds connect the C nuclei in-plane.
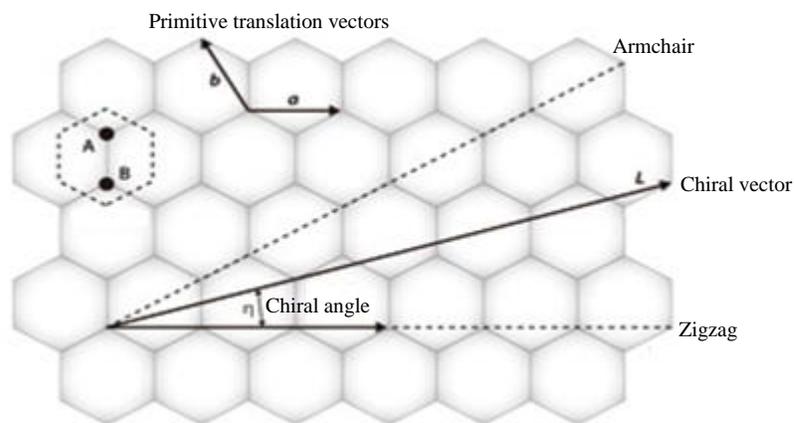

Figure 2.3: The honeycomb lattice of graphene. The hexagonal unit cell contains two carbon atoms (A and B). The chiral vector determining the structure of a carbon nanotube is given by L, and its length gives the circumference. The chiral angle is denoted by η, with $\eta = 0$ corresponding to zigzag nanotubes and $\eta = \pi/6$ to armchair nanotubes.

Electrical and electronic properties of nanotubes are affected by distortions like bending and twisting. Pentagon-heptagon pair is introduced in CNTs by bending, which results in metal-metal and semiconductor-metal nano scale junctions that can be used for nano-switches [19, 20]. The effect of bending becomes important when bending angles are more than 45º. At this stage kinks appear in the structure of the tube, resulting in reduction in conductivity of CNTs [21]. However, the presence of a metal nanowire inside the nanotube greatly suppresses the tube-buckling instability. In this case, increased tube diameter leads to an increase in the bending strength [22].

A model has been developed by Wang et al. [23] to study the elastic buckling of individual MWNTs under radial pressure. The critical pressure predicted by the model has been found in good agreement with the experimental results. A band gap opens upon twisting, which turns metallic CNTs to semiconducting. CNT structures collapse when twisted above a certain angle. Also, superconductivity in SWNTs has been observed but only at low temperatures [24]. Doping of CNTs provide various possibilities for controlling their physical properties. Doped CNTs possesses a variety of applications in nanoelectronics, spintronics, field emission, nonlinear optics, and chemical sensors [25]. CNTs align themselves along field lines under high electric fields, as shown in Figure 2.3. The relative magnitude of the field responsible for polarization and directed motion has been found to be dependent on the morphology of the nanotubes used. These observations may lead to novel electromechanical applications for CNTs [26].

It was found that temperature plays a key role in the strength of CNTs because motion of dislocations is thermally activated. CNTs are brittle at low temperature, irrespective of their diameter and helicity. However, CNTs exhibit flexibility at room temperature due to their high strength and the distortion capability of hexagonal network for relaxing stress [27]. At high temperature, spontaneous formation of double pentagon-heptagon pairs were observed in strained CNTs. It was found that such as defects depend on the chirality of CNTs and are energetically favored in defect-free armchair nanotubes when the tensile strain is greater than 5%. These defects constitute the onset of the possible plastic deformation of CNTs [28]. It is worth mentioning here that the high strength and high stiffness properties of an individual SWNTs does not necessarily imply that CNT structures will have the same properties [29].

2.4 Alcohol Sensor

Polypyrrole-polyvinyl alcohol and pure PPY gas sensors were prepared by in situ vapor state polymerization method. Both types of sensors had positive sensitivity when exposed to methanol gas. The sensitivity of PPY/PVA composite sensor was higher than that of pure PPY sensor. Mutually the response and recovery time of PPY/PVA composite sensors were longer than those of pure PPY sensors [30].

Metal oxide ethanol sensor prepared by ethanol vapor which is one of the most exhaustively studied gases. Metal oxide semiconductor, which is usually representing a property that the electrical conductivity varies with the composition of the gas atmosphere

surrounding it, is an extremely popular and useful sensing material for ethanol vapor sensing. Several oxide materials commonly used as ethanol gas sensors including pure and metal-doped e.g. SnO_2, In_2O_3, TiO_2, ZrO_2, WO_3, MoO_3, Cu_2O, and ZnO. ZnO gas sensing materials owe to their high chemical stability, low cost, and good flexibility in fabrication. The gas sensing mechanism involves chemisorptions of oxygen on the oxide surface followed by charge transfer during the reaction between chemisorbed oxygen reducing and target gas molecules [31].

An ethanol sensor based on ZnO nanorods prepared by hydrothermal method [32] has showed high sensitivity to ethanol concentration ranging from 10 to 2000 ppm at 330˚C with good response and recovery time. Furthermore, ZnO nanowire ethanol gas sensor showed high sensor signal and fast response to ethanol gas at concentration up to 200 ppm with operating temperature of 300˚C. In addition, pure ZnO nano-rode and nano-needles, which have been produced by hybrid induction and laser heating (HILH) technique, also showed capability to produce sensors with good sensing signal at a maximum temperature of around 400˚C for a concentration of 100 ppm of volatile organic compounds (VOCs) including acetone, toluene, and ethanol. In/ZnO system with In composition of 4.58% showed highest sensor signal compared to pure ZnO [33]. Moreover, AI/ZnO thin films were prepared by RF magnetron sputtering on Si substrate using Pt as interdigitated electrodes. The gas sensing results showed that the sensor signal for detection 400 ppm ethanol vapour was about 20 at an operating temperature of 250˚C [34].

ZnO nanoparticles were made by flame spray pyrolysis of zinc naphthenate in tolune and acetonitrile. The crystalline size of ZnO particles were found to be ranging from 10 to 20 nm and nanorode-like particles were found to be ringing from 10 to 20 nm in width and 20 to 50 nm in length. Sensing films about 5µm thick were doctor–bladed onto Al_2O_3 substrate interdigitated with Au electrodes used as ethanol gas sensors. The gas sensing performances of films were mainly investigated for ppm levels, (25-250 ppm) of ethanol with operating temperature of 400˚C. The cracking phenomenon is sensing layer could be improved by varying the heating conditions in terms of the annealing temperature and heating rate. It has been found that the sensor samples annealed using very fast heating rates showed serious cracks than slower heating rates. The sensors had n-type response to these vapors with response and recovery times within seconds or minutes [35].

2.5 Carbon Nanotube Based Sensors

Sensors are devices that detect or measure physical and chemical quantities such as temperature, pressure, sound, and concentration. The measurands are converted into an electrical signal. The main requirements of a good sensor are high sensitivity, fast response, low cost, high volume production, and high reliability. Sensors continue to make significant impact in everyday life with applications ranging from biomedical to automotive industry.

Multi-Walled Carbon Nanotubes (MWCNTs) used in this research is produced by means of Floating Catalyst Chemical Vapor Deposition (FC-CVD) technique, to investigate the

electronic sensor application of carbon nanotubes upon absorption of acetylene. According to the experimental results, it was proven that the carbon nanotubes have the capability to detect acetylene at room temperature. Therefore, it can be concluded that the gas sensing characteristics carried out in this work has shown that carbon nanotubes have the required potential to be an excellent acetylene sensor material at room temperature [36].

The signal of alcohol vapor is easily distinguishable from others due to the flow of compressed air and water as the response from 200 ppm alcohol vapor was about 100% larger than the other two kinds of vapor. Consequently, this confirms that the MWCNTs are really detecting alcohol molecules from the ethanol solution.

Carbon nanotube-based ethanol sensors have demonstrated the possibility of using metal–CNT hybrid materials as sensitive sensors of ethanol vapor at room temperature. Infiltration of different transition metals into the CNT resulted in sensors with varying sensitivity to ethanol. A phenomenal transition in sensitivity was observed at trace ethanol vapor concentration (1–10 ppm), from virtually no sensitivity at this level for the pristine SWNT sensor increases up to 100–5000 times for the metal CNT hybrid sensors. Apart from the Ni at CNT sensor, all hybrid sensors showed significantly improved response to ethanol vapor over a wide concentration range relative to the starting SWNT sensor. This is attributed to specific modification to the CNT electronic properties by the infiltrated transition metals. The varied responses to ethanol vapor offered by the metal CNT hybrids are attractive for creation of a sensitive and potentially selective multi-sensor array employing various

23

combinations of hybrid CNT materials. The result of a unique combinatorial response code produced by adsorption of ethanol vapor may then be used as positive identification for detection or discrimination of ethanol from a gas mixture [37].

Modified Carbon Nanotubes CNTs chemiresistors have been fabricated by CVD technology onto low-cost alumina substrates for chemical gas detection at room temperature. Surface modifications of CNTs network films with surface layers of metalloporphyrins (MPP) of zinc and manganese tetraphenylporphyrin resulted sensors with enhanced sensitivity and different selectivity. The variation of sensors resistance was recorded upon exposure at fixed concentration level of 5 min pulses of ethanol, ethylacetate, toluene, triethylamine and acetone at room temperature. It has been toted that the electrical resistance to modified carbon nanotube is higher than pure CNTs [38].

Modification of CNTs with polymers also improves their sensing properties toward vapors of organic compounds (VOCs). Abraham et al. [39] developed a compact wireless gas sensor based on a MWCNTs/ PMMA composite chemiresistor. The composite film was made by ultrasonication of MWCNTs and PMMA for 2 hours in dichloromethane and the chemiresistance were fabricated by dip-coating. The sensor shows fast response (2-5 seconds) and 10^2-10^3 order increase in resistance upon exposure to dichloromethane, chloroform and acetone vapors. It returns to the initial level immediately after removing the gas. The sensing mechanism was explained by swelling of the polymer due to absorption of organic vapors into the PMMA and the charge transfer when polar organic vapors adsorb

24

on the CNT surface. Solvents such as methanol, ethyl, acetate, and toluene, in which PMMA is insoluble or less soluble, also showed response. The polar nature of the solvents and the extent of interaction determine the response of the sensor.

Gas sensor based on nanostructure oxides modified MWCNTs have also been incorporated with SnO_2 for synthesized a compound material of MWCNTs coated with SnO_2 at ambient conditions [40]. The MWCNTs /SnO_2 sensor exhibited good sensing responses to liquefied petroleum gas (LPG) and ethanol (C_2H_5OH) vapor with fast response and recovery within seconds at temperature of 335˚C. Furthermore, the gas sensor response increased linearly with increment of gas concentration of LPG and ethanol. The high response and low resistance may be attributed to the particular electrical transport mechanism. The resistance of the sensor is dominated by the barriers among the SnO_2 grains on the MWCNTs. Electron travel through the SnO_2 grains into the MWCNTs, and then conduct in the MWCNTs with low resistance. Chen et al. [41] synthesized MWCNTs/SnO_2 core/shell nanostructures by a simple wet-chemical method. The thickness of the SnO_2 shell was about 10 nm and the diameters of the SnO_2 particles were 2-8 nm. Sensors based on the core/shell heterostructures exhibited enhanced ethanol sensing properties at working temperature of 300˚C. The response up to 50ppm ethanol was up to 24.5 and the response time and recovery time were about 1 and 10 seconds, respectively. In addition, the fluctuation of the response was less than +3% on remeasurement after 3 months.

2.6 Carbon Nanotube as Alcohol Sensor

Cross sectional structure of the FET-based sensor is illustrated in Figure 2.4. The drain current measurements as a function of time are shown in Figure 2.5. When the saturated ethanol vapor is delivered to the surface, a sharp spike is observed after a few seconds and then the current decreases and reaches a steady value. Recently, new chemical sensors based on single-stranded DNA (SS-DNA) as the chemical recognition site and SWNT field effect transistors as the electronic read-out component have been proposed by researchers of the same interests [42]. These sensors were able to detect variety of gases with rapid response and fast recovery times.
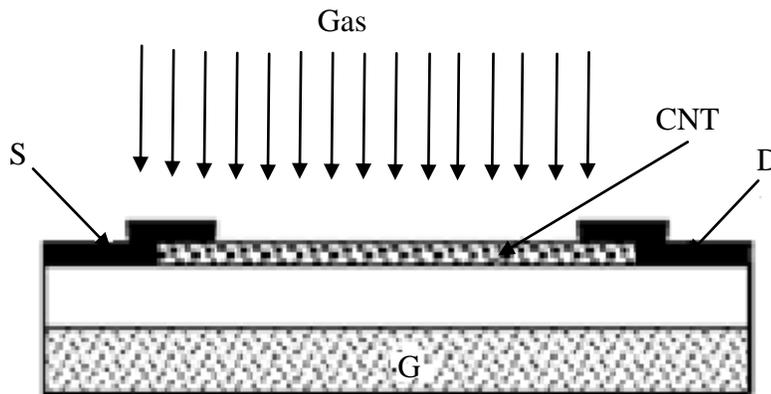
Figure 2.4: - Cross sectional structure of the FET-based sensor and the experimental geometry [43].

The schematic of the experimental setup and the employed gases in the experiment are shown in Figure 2.6. The change in sensor current upon exposure to different gases is

shown in Figure 2.7. These sensors are self-regenerating: samples maintain a constant response with no need for sensor refreshing for approximately 50 gas exposure cycles.
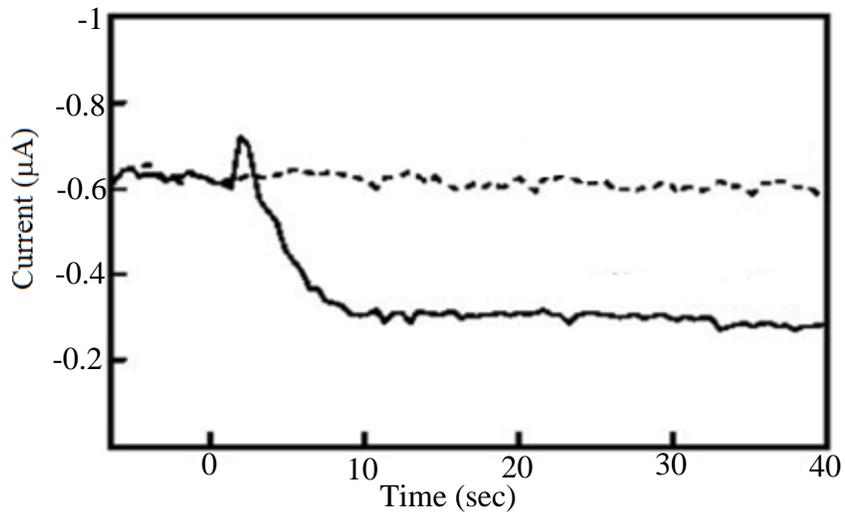

Figure 2.5: Illustrates the drain current measurements as a function of time with a source drain bias of 100 mV and a gate bias of 10 V [43].

These features make these sensors suitable for applications ranging from homeland security to disease diagnosis. In another study [44], an electrochemical sensing platform based on the integration of redox mediators and CNTs in a polymeric matrix has been developed by The incorporation of CNTs decreased the over potential for the mediated process by an extra 0.30 V and reduced the response time from 70 seconds to approximately 5 seconds.
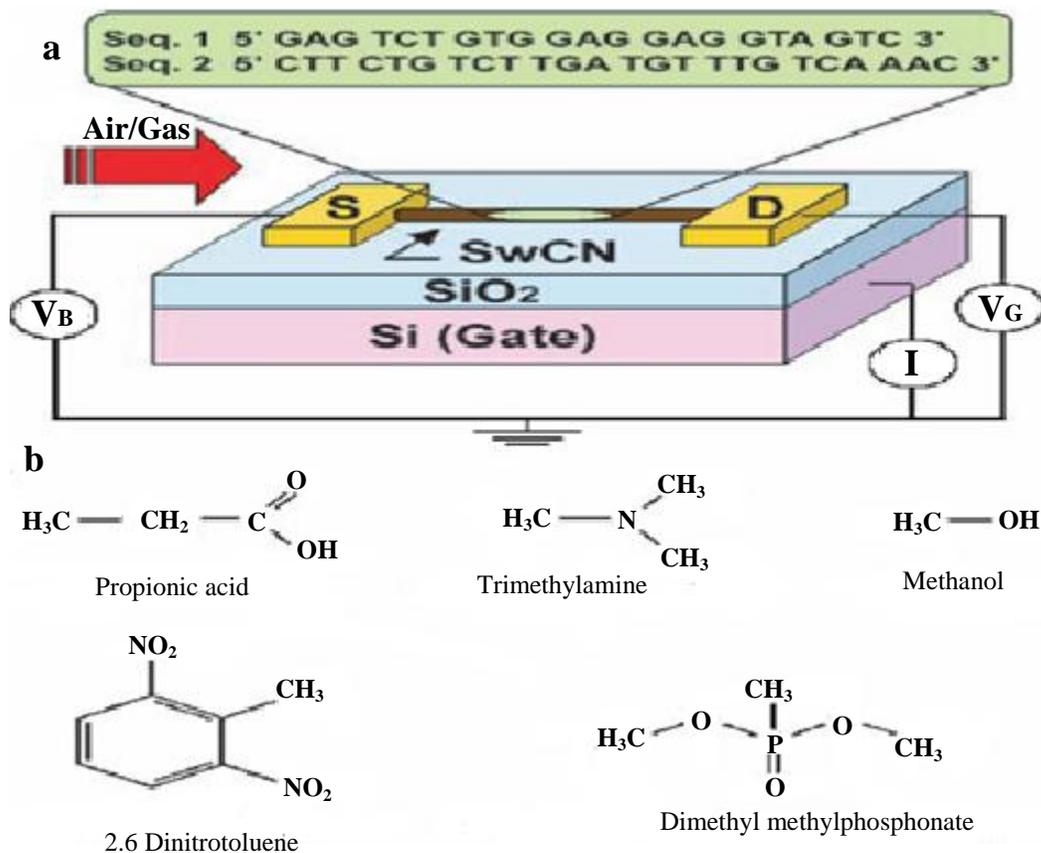
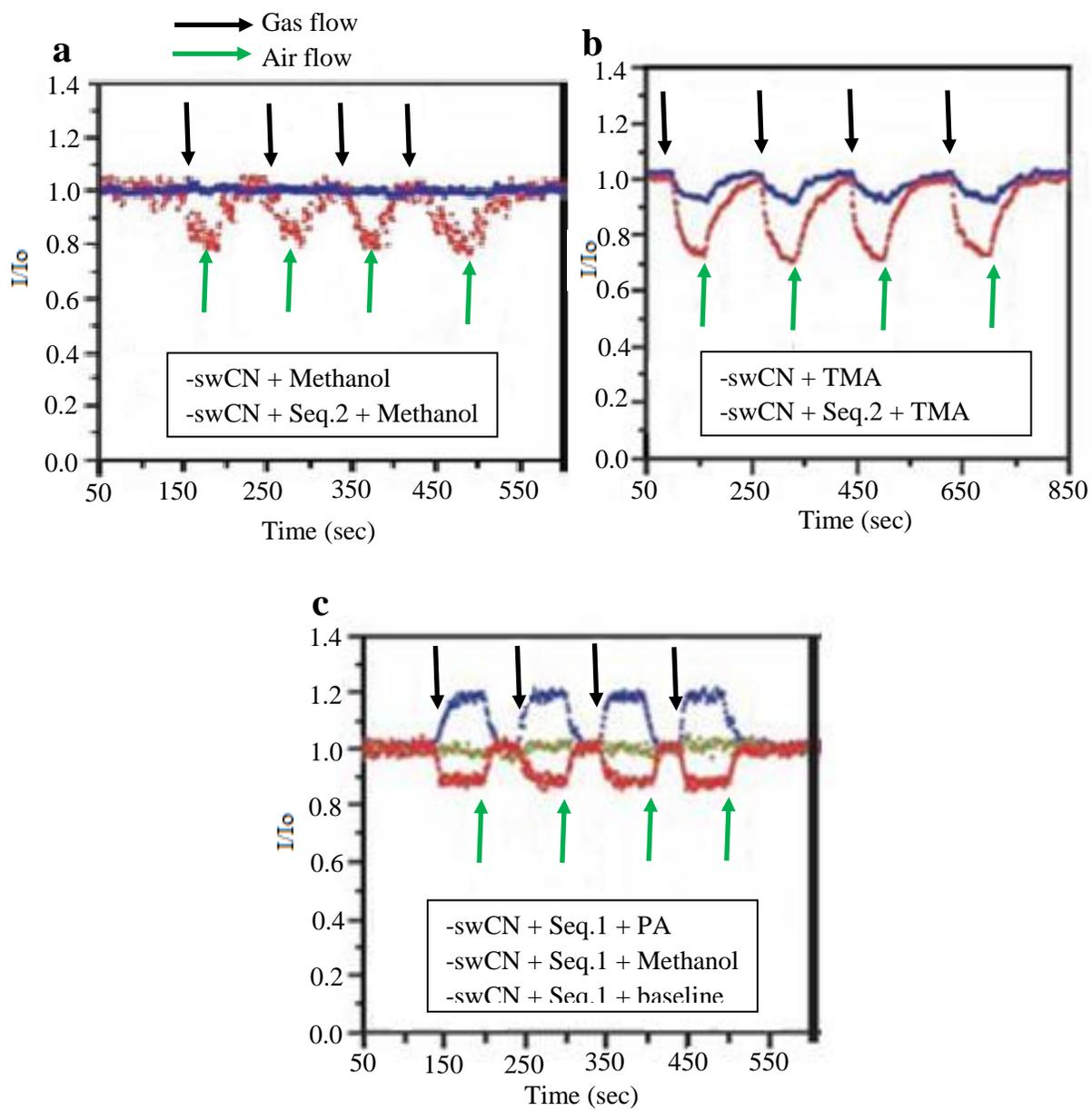Figure 2.6: - (a) Schematic diagram of experimental setup. (b) Gases used in the experiment [42].

Figure 2.7: - Change in sensor current upon exposure to different gases [42].

2.7 Instruments for the Characterization of Carbon Nanotube Composites

Several analytical techniques are used to characterize the CNT/ Polymer compsite such as Fourier Transform Infra-red spectrometry (FTIR), X-ray diffraction (XRD), scanning electron microscopy (SEM) and auger electron spectroscopy (AES).

2.7.1 Fourier Transform Infra-red Spectrometry (FTIR)

Fourier Transform Infra-red (FTIR) is the preferred method of infrared spectroscopy. In infra-red spectroscopy, IR radiation is passed through a sample. Some of the infra-red radiation is absorbed by the sample where the atoms of the sample gain energy and vibrate. This vibration creates a molecular fingerprint of the sample. Like a fingerprint no two unique molecular structures produce the same infra-red spectrum. This makes infrared spectroscopy useful for several types of analysis to provide extremely analytical useful information such as:

- It can identify unknown materials.

- It can determine the quality or consistency of a sample.

- It can determine the amount of components in a mixture.

Basic components of FTIR

The basic components of the Fourier Transform Infra-red (FTIR) spectroscopy is illustrated in Figure 2.8

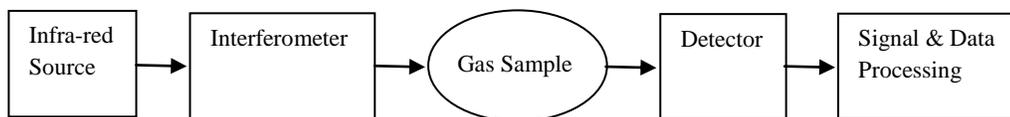| Infra-red Source | → | Interferometer | → | Gas Sample | → | Detector | → | Signal & Data Processing |

Figure 2.8: - Depicts the basic components of FTIR system.

Theory of Infra-red Absorption

At temperatures above absolute zero, all the atoms in the various molecules are in continuous vibration with respect to each other. When the frequency of a specific vibration is equal to the frequency of the IR radiation directed on the molecule, the molecule absorbs the radiation.

Each atom has three degrees of freedom, corresponding to motions along any of the three Cartesian coordinate axes (x, y, z). A polyatomic molecule of n atoms has $3n$ total degrees of freedom. However, 3 degrees of freedom are required to describe translation, the motion of the entire molecule through space. Additionally, 3 degrees of freedom correspond to rotation of the entire molecule. Therefore, the remaining $3n - 6$ degrees of freedom are true which are the fundamental vibrations for nonlinear molecules. Linear molecules possess $3n - 5$ fundamental vibration modes because only 2 degrees of freedom are sufficient to describe rotation. Among the $3n - 6$ or $3n - 5$ fundamental vibrations (also known as normal modes of vibration), those that produce a net change in the dipole

moment may result in an IR activity and those that give polarizability changes may give rise to Raman activity.

Naturally, some vibrations can be both IR- and Raman-active. The total number of observed absorption bands is generally different from the total number of fundamental vibrations. It is reduced because some modes are not IR active and a single frequency can cause more than one mode of motion to occur. Conversely, additional bands are generated by the appearance of overtones (integral multiples of the fundamental absorption frequencies), combinations of fundamental frequencies, differences of fundamental frequencies, coupling interactions of two fundamental absorption frequencies, and coupling interactions between fundamental vibrations and overtones or combination bands (Fermi resonance). The intensities of overtone, combination, and difference bands are less than those of the fundamental bands. The combination and blending of all the factors thus create a unique IR spectrum for each compound.

The major types of molecular vibrations are stretching and bending. The various types of vibrations are illustrated in Figure 2.9. Infra-red radiation is absorbed and the associated energy is converted into these types of motions. The absorption involves discrete, quantized energy levels. However, the individual vibration motion is usually accompanied by other rotational motions. These combinations lead to the absorption bands, not the discrete lines, commonly observed in the mid IR region [45].
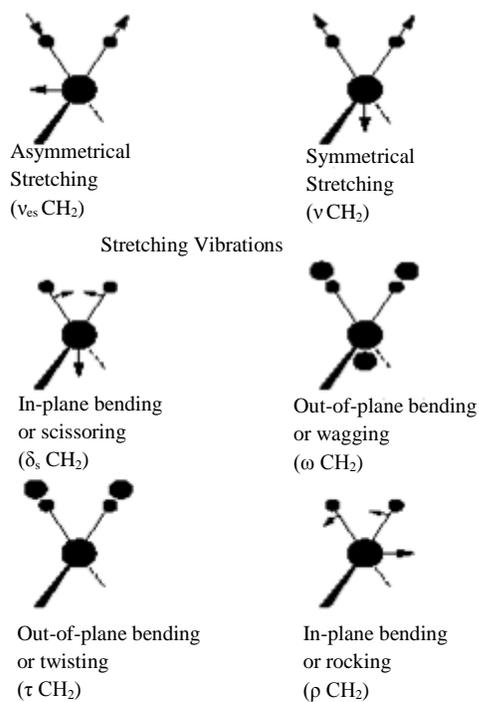
Asymmetrical
Stretching
(ν_{es} CH$_2$)

Symmetrical
Stretching
(ν CH$_2$)

Stretching Vibrations

In-plane bending
or scissoring
(δ_s CH$_2$)

Out-of-plane bending
or wagging
(ω CH$_2$)

Out-of-plane bending
or twisting
(τ CH$_2$)

In-plane bending
or rocking
(ρ CH$_2$)

Figure 2.9: - Major vibration modes for a nonlinear group.

FTIR Characterisation of Functionalised Carbon Nanotubes

Multi-walled carbon nanotubes dispersed by optical tweezers were functionalized as evident by their FTIR spectra shown in Figure 2.10. The FTIR spectra of functionalized multi-walled carbon nanotubes showed three additional transmittance peaks at 1739.4 cm^{-1}, 3430.9 cm^{-1}, and 1638.2 cm^{-1} compared with control spectrum.
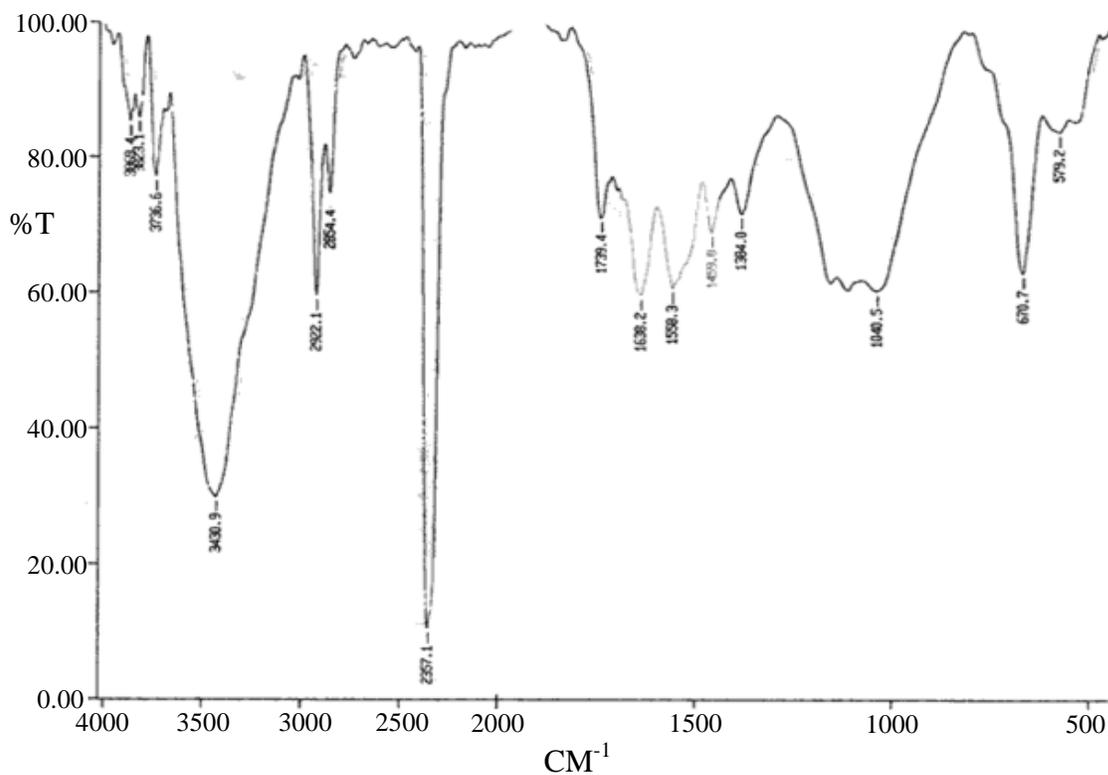
Figure 2.10: - FTIR spectra of functionalized carbon nanotubes.

These three peaks correspond to carboxyl group (stretching), hydroxyl group (stretching) and carbonyl (stretching) functional groups respectively. The peak at 3430 cm^{-1} (lower intensity) was also observed in the control spectrum and is caused by moisture in the sample. Two major peaks at 2919.2 cm^{-1} and 2354.8 cm^{-1} were also seen in the spectrum. The origin of these peaks attribute to the parylene and CO_2 coating of the IR optics in the spectrometer respectively [46].

2.7.2 Fundamental Principle of X-ray Diffraction (XRD)

Diffraction is a scattering phenomenon when x-rays are incident on crystalline solid, they are scattered in all directions. In some of these directions, the scattered beams are completely in phase and reinforce one another to form the diffracted beams. The Bragg law describes the conditions under which this would occur. It is assumed that a perfectly parallel and monochromatic x-ray beams of wavelength λ is incident on a crystalline sample at angle θ.
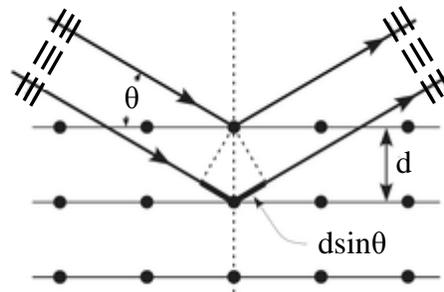

Figure 2.11: - X-ray Diffraction analysis.

Diffraction will occur if the following equation satisfied in order to acquire constructive interference.

$$n\,\lambda = 2d\,\sin\theta \qquad\qquad (2.1)$$

Where,

d is distance between atomic planes

n is an integer (1,2,…,n)

λ the incident x-ray beam wavelength and

θ the angle of incidence of the x-ray beam and the atomic planes.

2dsinθ is the path length difference between two incident x-ray beams where one x-ray beam takes a longer, but parallel, path because it "reflects" off an adjacent atomic plane. This path length difference must equal an integer value of the λ of the incident x-ray beams for constructive interference to occur such that a reinforced diffracted beam is produced.

By varying the angle θ, the Bragg's Law conditions are satisfied by different d-spacing in polycrystalline materials. Plotting the angular positions and intensities of the resultant diffracted peaks of radiation produces a pattern, which is characteristic of the sample. Where a mixture of different phases is present, the resulting diffractogram is formed by addition of the individual patterns. Based on the principle of X-ray diffraction, significant information of structural, physical and chemical bonding about the investigated material can be obtained.

For a given λ of incident x-rays and a particular inter-planar spacing (d), in a given material sample, only specific θ angles will satisfy the Bragg equation. No "reflections"

will occur until the incident beam makes an angle θ that satisfies the Bragg equation with n

= 1. Continued rotation leads to other "reflections" at higher values of θ correspond to an

integer value of n (n = 2, 3, etc.); these known as 1st, 2nd, 3rd order, etc., of "reflections"

X-Ray Diffraction (XRD)

X-ray diffraction provides information about crystalline size, chemical composition,

and phase identifies the structural properties (interlayer distance, stream and impurities) in

both film and powder forms [47, 48].

Incident
X-ray beam

Diffracted beam
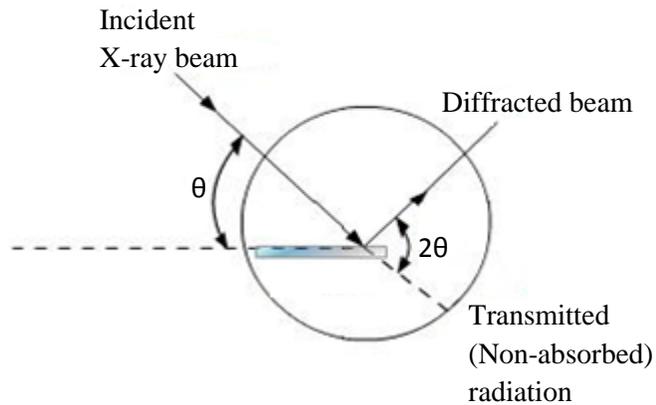
θ

2θ

Transmitted
(Non-absorbed)
radiation

Figure 2.12: - Diagram of X-ray diffractometer.

X-ray diffraction of a particular sample is obtained when a beam of X-ray diffracted at the crystalline compound is scattered satisfying Bragg's law. The diffraction and intensity of the diffracted beams depend on the orientation of the crystal lattice. Hence, the scattering angle is always twice of glancing angle. The identification of an unknown sample can be easily achieved by comparing its x-ray diffractogram with globally-standard recognized database, which is usually operated by automatic routines in a computer-controlled system.

For Example:

Heat Treated Sample Structures of γ-Fe$_2$O$_3$ and γ-Fe$_2$O$_3$ –TiO$_2$, at 400°C.

Figure 2.13 shows the XRD patterns of γ-Fe$_2$O$_3$ and γ-Fe$_2$O$_3$ –TiO$_2$ heat treated at 400°C. XRD patterns reveal that the first sample (Fig. 2.13a) is a mixture of two phases, maghemite M (γ-Fe$_2$O$_3$) and hematite H (α-Fe$_2$O$_3$). This means that a phase transition from spinal structure (γ-Fe$_2$O$_3$) to corundum structure (α-Fe$_2$O$_3$) occurs by heating the material at a temperature of 400°C in agreement with other researchers of the same interest [48]. The second sample (Fig. 2.13b) is a mixture of three phases: γ-Fe$_2$O$_3$, α-Fe$_2$O$_3$ and anatase (A)-type TiO$_2$ phase. From XRD, data printed to obtain the lattice parameters, average size of the crystalline blocks and micro-strains as tabulated in table 2.1. It has been observed that both samples have a nanogranular structure and the average size of crystalline blocks decreases as revealed in table 2.1.

Table 2.1: - Phase composition, lattice constants (a, b, c), average size of the crystalline blocks (D) and micro-strains of heat treated γ-Fe_2O_3 and γ-Fe_2O_3 –TiO_2 samples at 400˚C

Sample	Phase Composition	Average size D [nm]	Micro-strains	Lattice constants [nm]
γ-Fe_2O_3	Hematite (H)	54.44	0.00314	a = b = 0.50409; c = 1.37701
	Maghemite (M)	129.96	0.00166	a = b = c = 0.83426
γ-Fe_2O_3 – TiO_2	Hematite (H)	38.61	0.002298	a = b = 0.50356; c = 1.37468
	Maghemite (M)	76.29	0.001448	a = b = c = 0.83434
	Anatase (A)	97.92	0.000971	a = b = 0.37867; c = 0.95142

a)
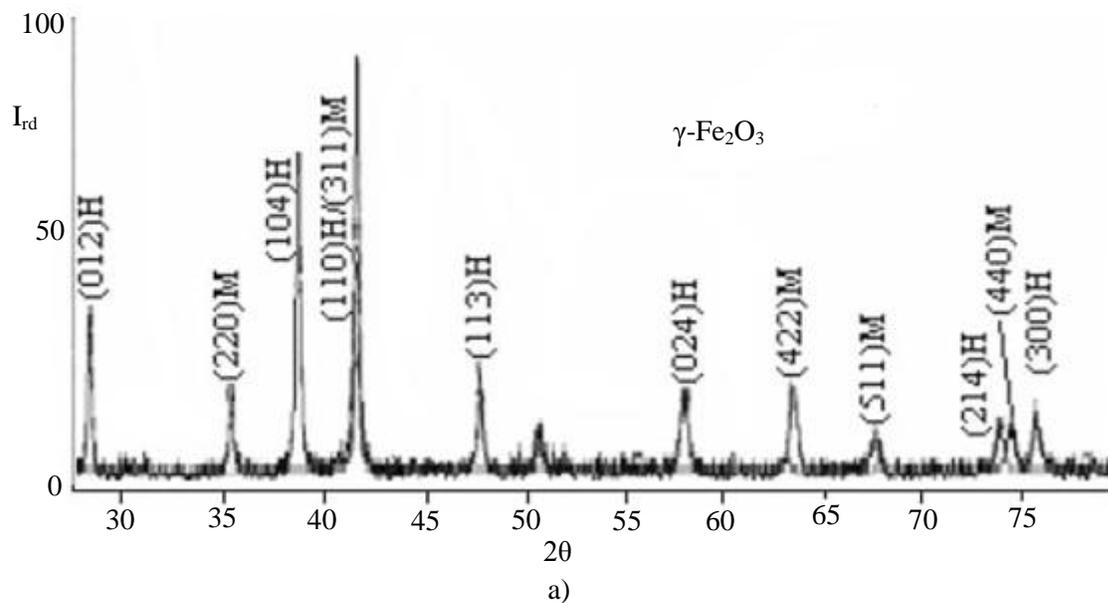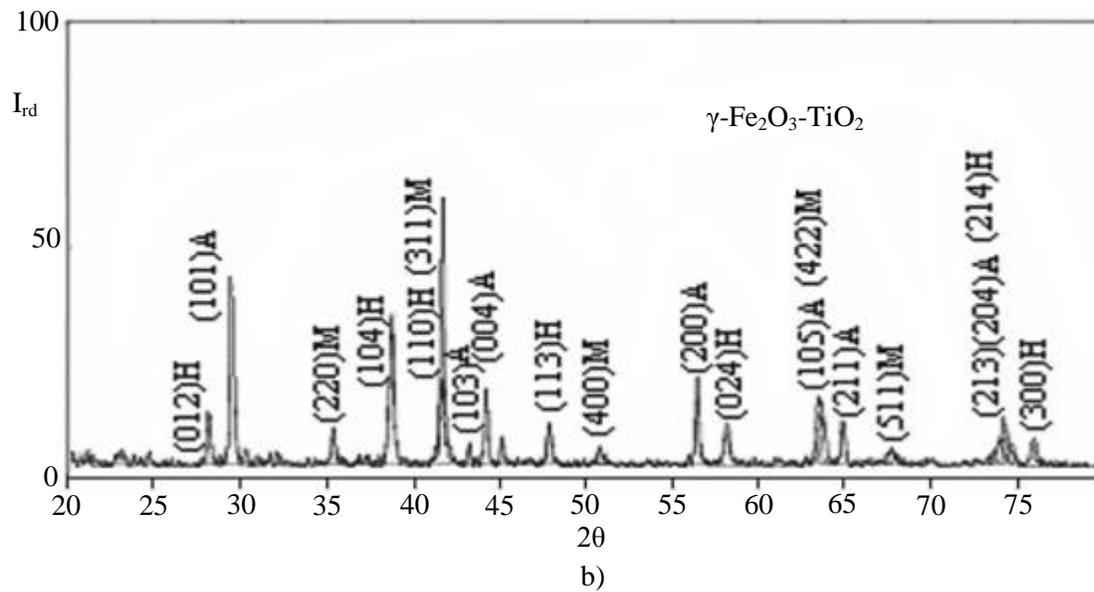
Figure 2.13: - XRD patterns of (a) γ-Fe$_2$O$_3$ and (b) γ-Fe$_2$O$_3$ –TiO$_2$ after heat treatment at a temperature of 400°C for 1 hour, (M – maghemite, H – hematite, A – anatase) [49].

Refrences: -

1. S. Ijima, *Nature* 354, 56 (1991).

2. S. Ijima and T. Ichihashi, *Nature* 363, 603 (1993).

3. D. S. Bethune, C. H. Kiang, M. S. De Vries, G. Gorman, R. Sa voy, J. V. Azquez, and R. B. Yers, *Nature* 363, 305 (1993).

4. T.W. Ebbesen and P. M. Ajayan, *Nature* 358, 220 (1992).

5. C. Journet, W. K. Maser , P. Bernier , A. Loiseau, M. L. De la Chapelle, S. Lefrant, P. Deniard, R. Lee, and J. E. Fischer , *Nature*388, 756 (1997).

6. A. Thess, R. Lee, P. N. Olaev, H. J. Dai, P. Petit, J. Robert, C. H. Xu, Y. H. Lee, S. G. Kim, A. G. Rinzler, D. T. Colbert, G. E. Scuseria, D. T. Omanek, J. E. Fischer, and R. E. Smalley, *Science* 273, 483 (1996).

7. S. Arepalli, P. N. Olaev, W. Holmes, and B. S. Files, *Appl. Phys. Lett.* 78, 1610 (2001).

8. C. D. Scott, S. Arepalli, P. N. Olaev, and R. E. Smalley, *Appl. Phys. A* 72, 573 (2001).

9. N. Braidy, M. A. El Khakani, and G. A. Botton, *J. Mater. Res.* 17, 2189 (2002).

10. S. Takahashi, T. Ikuno, T. Oyama, S. I. Honda, M. Katayama, T. Hirao, and K. Oura, *J. Vac. Soc. Jpn.* 45, 609 (2002).

11. M. J. Yacaman, M. M. Yoshida, L. Rendon, and J. G. Santiesteban, *Appl. Phys. Lett.* 62, 202 (1993).

12. V. K. Varadan and J. Xie, *Smart Mater. Struc.* 11, 610 (2002).

13. D. Park, Y. H. Kim, and J. K. Lee, *Carbon* 41, 1025 (2003).

14. R. Seidel, G. S. Duesberg, E. Unger, A. P. Graham, M. Liebau, and F. Kreupl, *J. Phys. Chem. B* 108, 1888 (2004).

15. J. K. Vohs, J. J. Brege, J. E. Raymond, A. E. Brown, G. L. Williams, and B. D. Fahlman, *J. Am. Chem. Soc.* 126, 9936 (2004).

16. B. Q. Wei, R. Vajtai, Y. Jung, J. Ward, R. Zhang, G. Ramanath, and P. M. Ajayan, *Nature* 416, 495 (2002).

17. S. Chaisitsak, A. Yamada, and M. Konagai, *Diam. Rel. Mater.* 13, 438 (2004).

18. S. Maheshwar, P. R. Apte, S. C. Purandare, and R. Zacharia, *J. Nanosci. Nanotechnol.* 5, 288 (2005).

19. P. Lambin, J. P. Vigneron, A. Fonseca, J. B. Nagy, and A. A. Lucas, *Synth. Met.* 77, 249 (1996).

20. L. Chico, V. H. Crespi, L. X. Benedict, S. G. Louie, and M. L. Cohen, *Phys. Rev. Lett.* 76, 971 (1996).

21. A. Rochefort, D. R. Salahub, and P.Avouris, *Chem. Phys. Lett.* 297, 45 (1998).

22. D. Danailov, P. Keblinski, S. Nayak, and P. M. Ajayan, *J. Nanosci. Nanotechnol.* 2, 503 (2002).

23. A. Rochefort, P. Avouris, F. Lesage, and D. R. Salahub, *Phys Rev. B* 60, 13824 (1999).

24. M. Kociak, A.Y. Kasimov, S. Gueron, B. Reulet, I. I. Khodos, Y. B. Gorbatov, V. T. Volkov, L.Vaccarini, and H. Bouchiat, *Phys. Rev. Lett.* 86, 2416 (2001).

25. J. Zhaoa and R. H. Xieb, *J. Nanosci. Nanotechnol.* 3, 459 (2003).

26. N. Koratkar, A. Modi, J. Kim, B. Q. Wei, R. Vajtai, S. Talapatra, and P. M. Ajayan, *J. Nanosci. Nanotechnol.* 4, 69 (2004).

27. J. P. Salvetat, J. M. Bonard, N. H. Thomson, A. J. Kulik, L. Forro, W. Benoit, and L. Zuppiroli, *Appl. Phys. A* 69, 255 (1999).

28. M. B. Nardelli, B. I. Yakobson, and J. Bernholc, *Phys. Rev. B* 57, R4277 (1998).

29. R. S. Ruoff, D. Qian, and W. K. Liu, *C. R. Physique* 4, 993 (2003).

30. L. Jiang, H. K. Jun, Y. S. Hoh, J. O. Limc, D. D. Lee, J. S. Huh, Sensors and Actuators B 132–137 105 (2005).

31. Y. Wang and J. T. W. Yeow, Journal of Sensors Volume, Article ID 493904, p. 24 (2009).

32. Q. Wan, Q. H. Li, Y. J. Chen, X. L. He, J. P. Li, C. L. Lin, T. H. Wang, *Appl. Phys. Lett.* 84, p.3654-3656, (2004).

33. B. L. Zhu, D. W. Zeng, J. Wu, W. L. Song, C. S. Xie, *J. Mater. Sci.-Mater. Electron.* 14, p.521-52, (2003).

34. S. M. Chou, L. G. Teoh, W. H. Lai, Y. H. Su, M. H. Hon, *Sensor* 2006, Vol. 6, p. 1420-1427 (2007).

35. C. Liewhiran and S. Phanichphant , sensor, ISSN 1424-8220,(2007).

36. M. Y. Faizah, A. Fakhru'l-Razi, R. M. Sidek, M. M. R. Naim. Journal of Engineering Science and Technology Vol. 3, p.71–78. No. 1 (2008).

37. S. Brahim1, S. Colbern, R. Gump, A. Moser and L. Grigorian. Nanotechnology 235502, p.20 (2009).

38. M. Penzaa, R. Rossia, M. Alvisia, M. A. Signorea, E. Serraa, R. Paolesseb, A. D'Amicoc, C. D. Natalec, Sensors and Actuators B (2009).

39. J. K. Abraham, B. Philip, A. Witchurch, V. K. Varadan, and C. C. Reddy, *Smart Materials and Structures*, vol. 13, no. 5, p. 1045–1049 (2004).

40. B. Y. Wei, M. C. Hsu, P. G. Su, H. M. Lin, R. J. Wu, and H. J. Lai, *Sensors and Actuators B*, vol.101, no. 1-2, p. 81–89 (2004).

41. Y. Chen, C. Zhu, and T. Wang, vol. 17, no. 12, p. 3012–3017 (2006).

42. C. Staii et al., *Nano Lett.* 5, American Chemical Society, p.1774 (2005).

43. T. Someya et al., *Nano Lett.* American Chemical Society, Vol.3, p.877 (2003).

44. M. Zhang and W. Gorski, *Anal. Chem. Vol.* 77, p.3960 (2005).

45. C. P. Sherman Hsu, Ph.D. Thesis, Separation Sciences Research and Product Development Mallinckrodt, Inc. Mallinckrodt Baker Division.

46. S. Kumar, R. Kumbar, R. Sinyth, A. K. Shukla, V. K. Jindal and L. M. Bharadwaj, Journal of Nanotechnology online (2006).

47. B. D. Cullity, Elements of X- ray Diffraction, Addison-Wesley Publishing Company, Inc. (1956).

48. T. Belin and F. Epron, Review: Characterization Methods of Carbon Nanotubes, Material Science and Engineering, p.1-4,(2005).

49. N. Rezlescu, C. Doroftei, E. Rezles, M. L. Craus, *Romanian Reports in Physics, Vol. 60,* No. 4, P. 1041–1052, (2008).